The ALFALFA Almost-Dark Galaxy AGC 229101: A Two Billion Solar Mass HI Cloud with a Very Low Surface Brightness Optical Counterpart

Lukas Leisman,[1,2] Katherine L. Rhode,[3] Catherine Ball,[4,5] Hannah J. Pagel,[3] John M. Cannon,[4] John J. Salzer,[3] Steven Janowiecki,[6] William F. Janesh,[7] Gyula I. G. Józsa,[8,9] Riccardo Giovanelli,[5] Martha P. Haynes,[5] Elizabeth A. K. Adams,[10,11] Laurin Gray,[3] and Nicholas J. Smith[3]

[1] *Department of Physics and Astronomy, Valparaiso University, 1610 Campus Drive East, Valparaiso, IN 46383, USA*
[2] *Department of Astronomy, University of Illinois, 1002 W. Green St., Urbana, IL 61801, USA*
[3] *Department of Astronomy, Indiana University, 727 East Third Street, Bloomington, IN 47405, USA*
[4] *Department of Physics & Astronomy, Macalester College, 1600 Grand Avenue, Saint Paul, MN 55105*
[5] *Cornell Center for Astrophysics and Planetary Science, Space Sciences Building, Cornell University, Ithaca, NY 14853, USA*
[6] *University of Texas, Hobby-Eberly Telescope, McDonald Observatory, TX 79734, USA*
[7] *Department of Astronomy, Case Western Reserve University, 10900 Euclid Avenue, Cleveland, OH 44106, USA*
[8] *South African Radio Astronomy Observatory, 2 Fir Street, Black River Park, Observatory, Cape Town, 7925, South Africa*
[9] *Department of Physics and Electronics, Rhodes University, PO Box 94, Makhanda, 6140, South Africa*
[10] *ASTRON, Netherlands Institute for Radio Astronomy, Oude Hoogeveensedijk 4, 7991 PD Dwingeloo, The Netherlands*
[11] *Kapteyn Astronomical Institute, University of Groningen, Landleven 12, 9747 AD, Groningen, The Netherlands*

(Received January 20, 2021; Accepted September 24, 2021)

ABSTRACT

We present results from deep H I and optical imaging of AGC 229101, an unusual H I source detected at v_{helio} = 7116 km s^{-1} in the ALFALFA survey. Initially classified as a candidate "dark" source because it lacks a clear optical counterpart in SDSS or DSS2 imaging, AGC 229101 has $10^{9.31\pm0.05} M_\odot$ of H I, but an H I line width of only 43±9 km s^{-1}. Low resolution WSRT imaging and higher resolution VLA B-array imaging show that the source is significantly elongated, stretching over a projected length of ∼80 kpc. The HI imaging resolves the source into two parts of roughly equal mass. WIYN pODI optical imaging reveals a faint, blue optical counterpart coincident with the northern portion of the H I. The peak surface brightness of the optical source is only $\mu_g \sim 26.6$ mag arcsec^{-2}, well below the typical cutoff that defines the isophotal edge of a galaxy, and its estimated stellar mass is only $10^{7.32\pm0.33} M_\odot$, yielding an overall neutral gas-to-stellar mass ratio of $M_{HI}/M_* = 98^{+111}_{-52}$. We demonstrate the extreme nature of this object by comparing its properties to those of other H I-rich sources in ALFALFA and the literature. We also explore potential scenarios that might explain the existence of AGC 229101, including a tidal encounter with neighboring objects and a merger of two dark H I clouds.

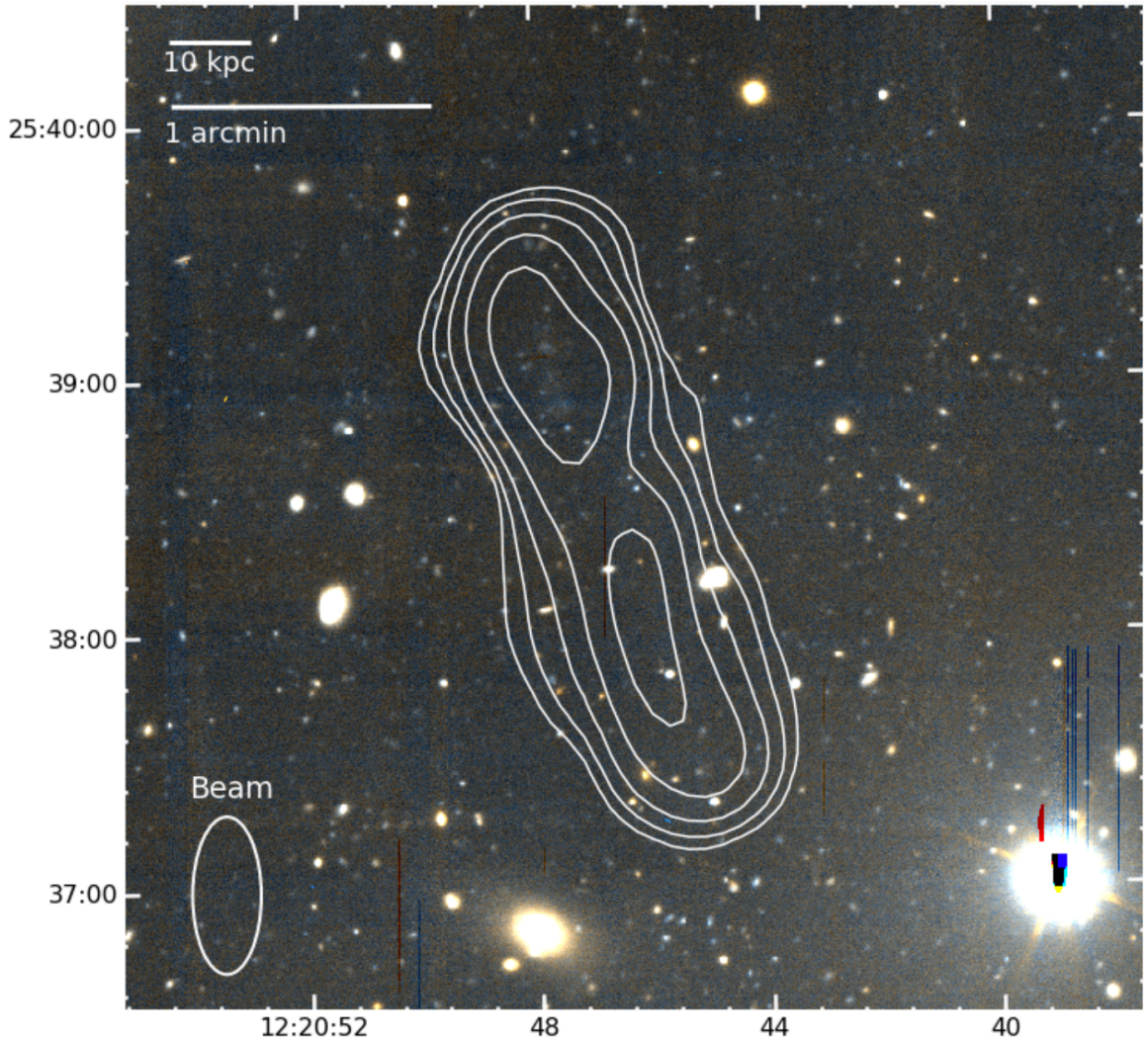

Figure 1. WIYN 3.5-m pODI combined g- and r-band color image of AGC 229101 with H I column density contours from WSRT only imaging at 1, 2, 4, 8, and 16 $\times 10^{19}$ cm^{-2} overlaid in white. The image is oriented N-up, E-left. Faint, diffuse optical emission is barely visible at the location of the northern H I column density peak, while the H I emission stretches over $\sim$80 kpc. The early-type galaxy to the southeast of AGC 229101 is unrelated and has an SDSS redshift of 0.176.

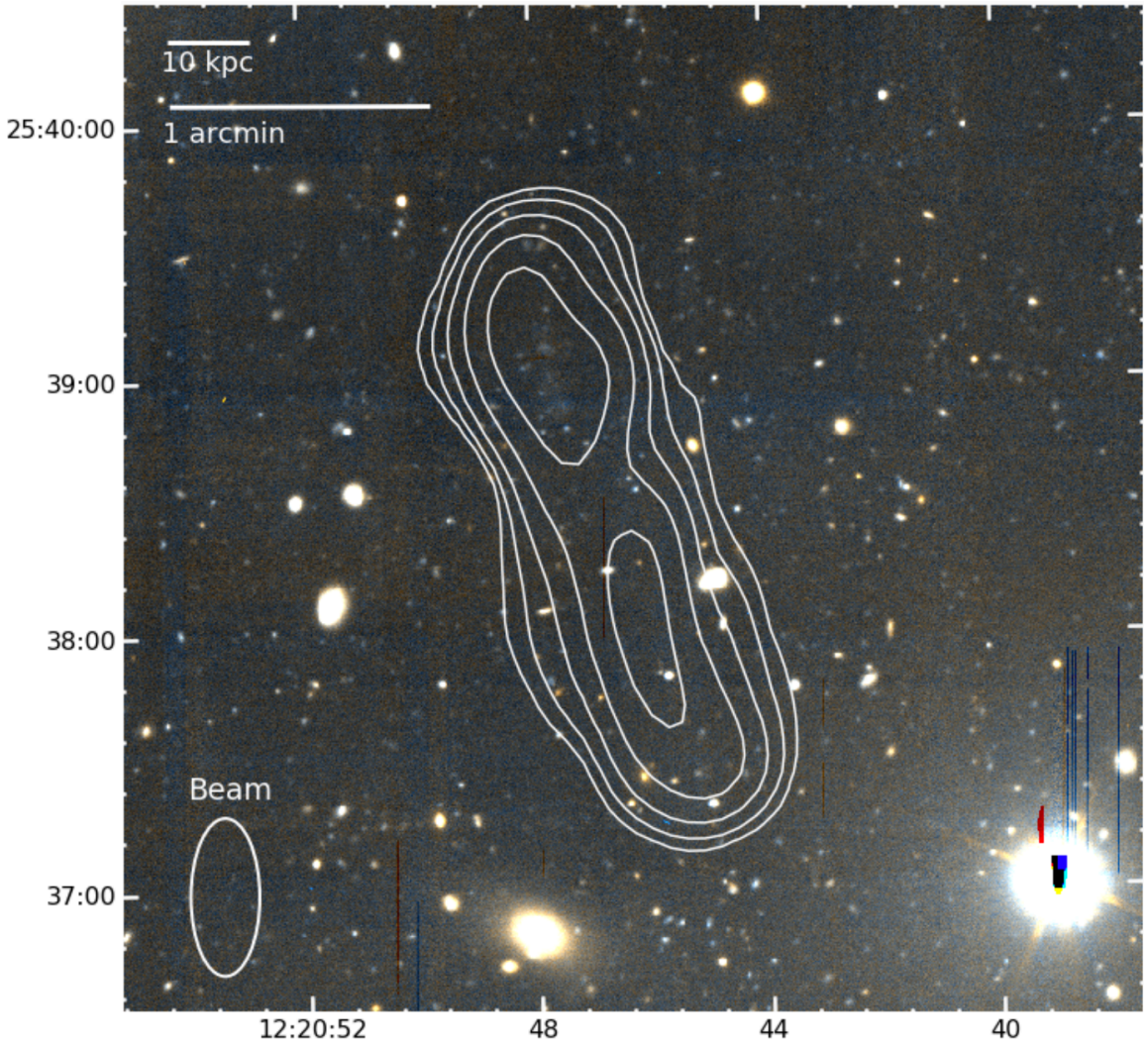

Figure 1. WIYN 3.5-m pODI combined g- and r-band color image of AGC 229101 with H I column density contours from WSRT only imaging at 1, 2, 4, 8, and 16 $\times 10^{19}$ cm^{-2} overlaid in white. The image is oriented N-up, E-left. Faint, diffuse optical emission is barely visible at the location of the northern H I column density peak, while the H I emission stretches over ∼80 kpc. The early-type galaxy to the southeast of AGC 229101 is unrelated and has an SDSS redshift of 0.176.

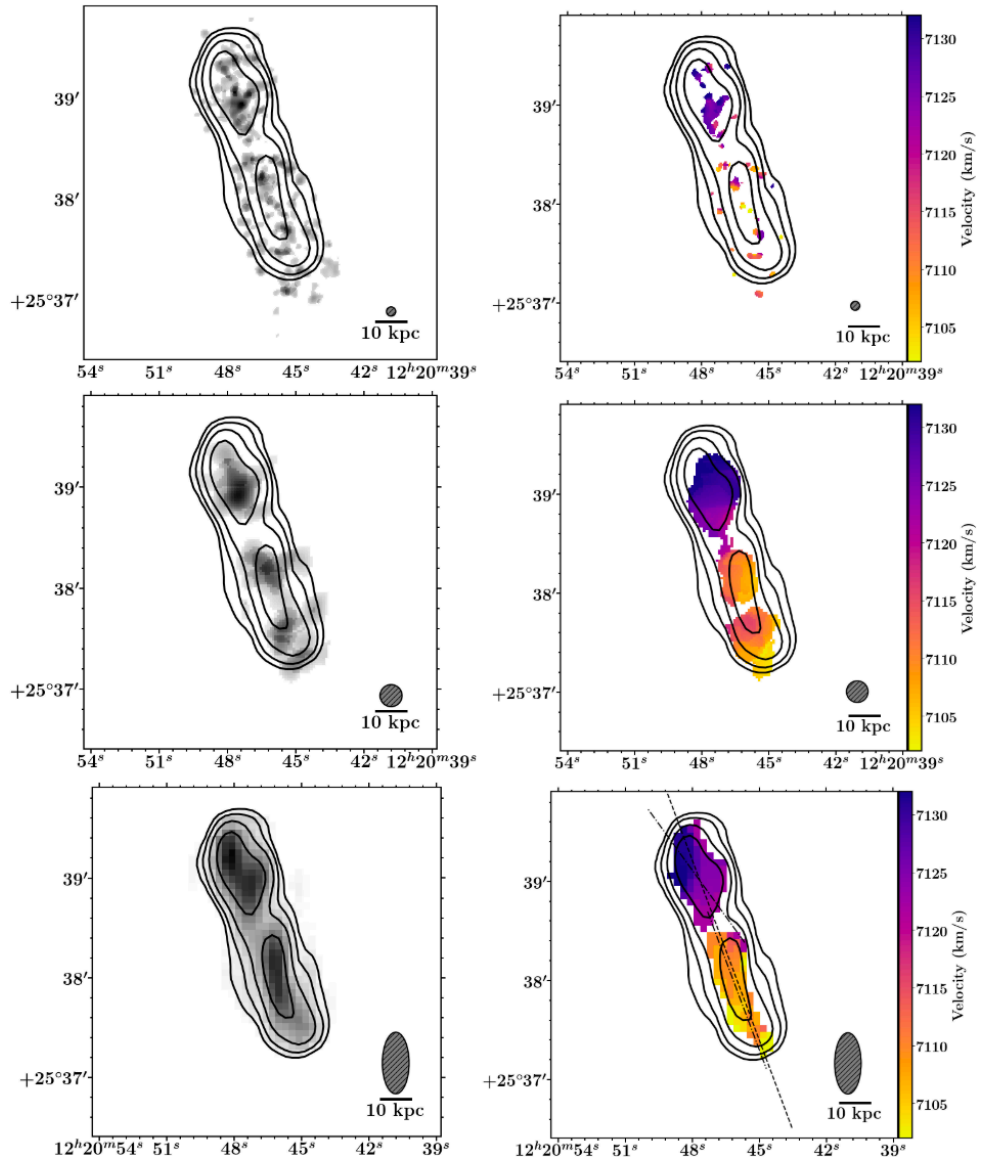

Figure 2. Left panels: H I moment zero column density maps at high- (top: 5.5″ beam), mid- (center: 13.1″ beam) and low-resolutions (bottom: 16×37″ beam). The high and mid resolution maps are from combined VLA B-array and WSRT imaging, and the low resolution map is from WSRT only, Briggs r=0.4 imaging. Beam sizes are shown with hashed gray circles in the lower right on each plot. The column density scale in the top image is 0.5-4.5×10^{20}atoms cm^{-2}, and is 0.15-3.2×10^{20}atoms cm^{-2} in the center image. Column density contours spaced in powers of 2 from 0.2-1.6×10^{20}atoms cm^{-2} from the WSRT moment 0 map are shown on all plots for direct comparison. Moment maps are masked to only include emission detected above 2σ, as discussed in the text. Right panels: Corresponding moment one velocity maps from combined VLA and WSRT (top and center), and WSRT only (bottom), imaging. Resolutions correspond to those of the moment zero maps to the left, masked at the 5σ level to highlight the motions of the highest signal-to-noise gas. The dashed line in the lower right panel shows the location of the position velocity slice shown in Figure 3, and the dot dashed lines show the locations of the northern and southern PV slices in Figure 3.

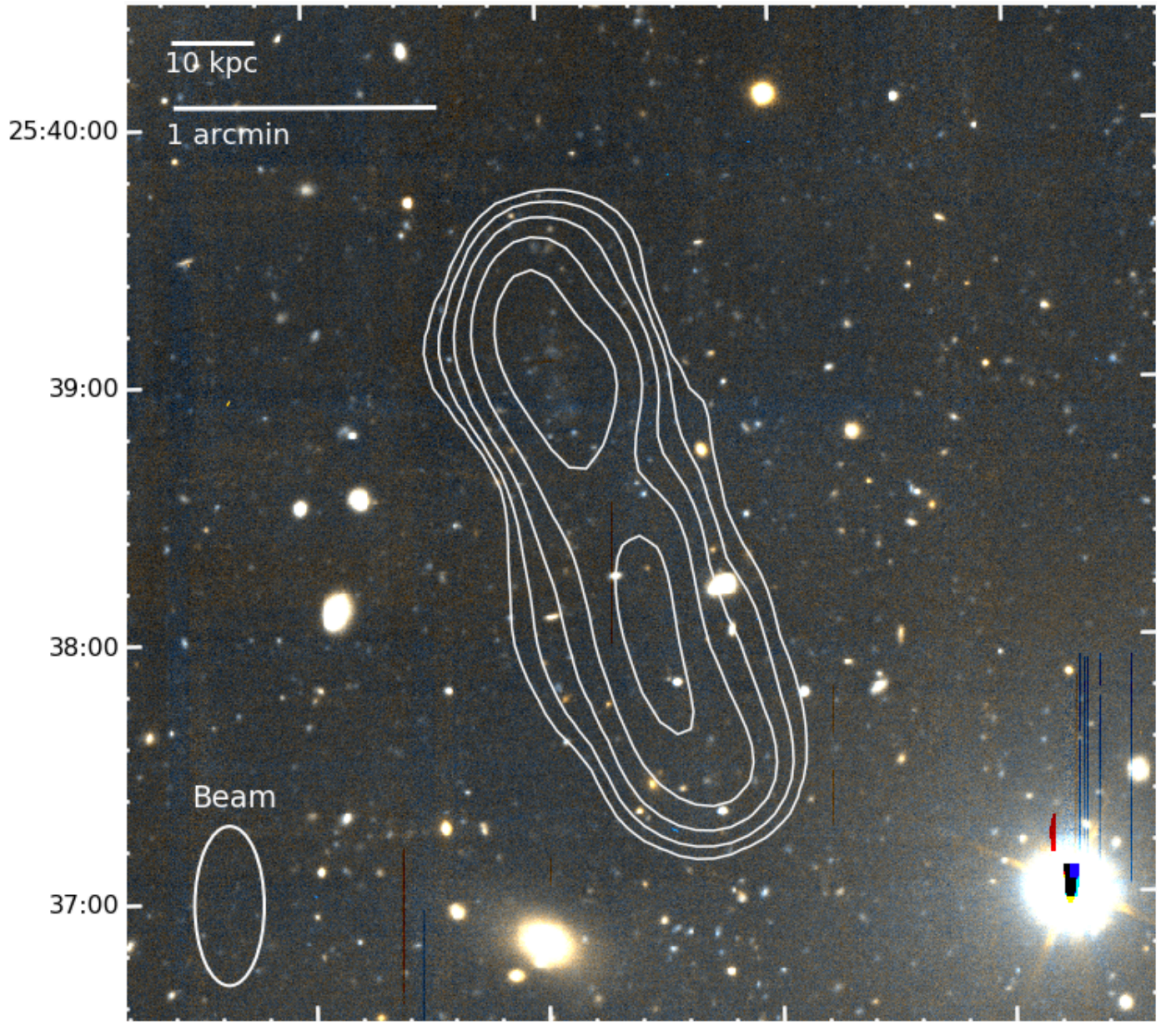

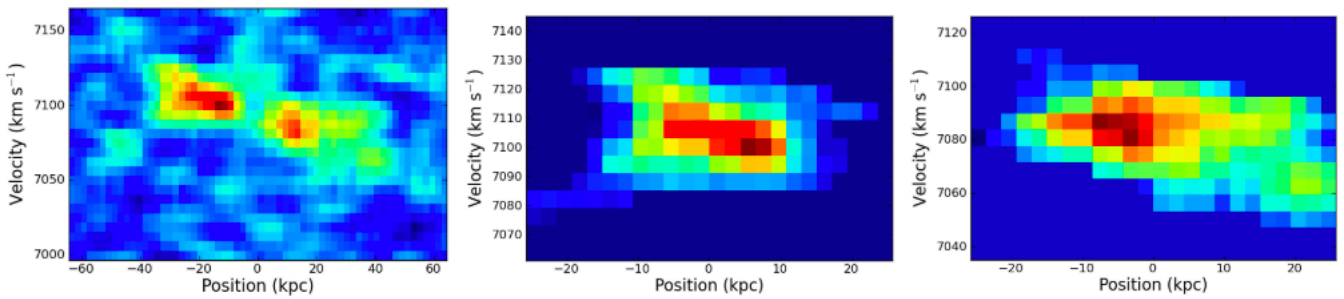

Figure 3. Position velocity slices made along the major axis of the WSRT (lowest resolution) data. Slices for each are 10″ wide. The left panel shows the position versus velocity plot across the full extent of the source; the central panel shows just the northern portion of the source, and the right hand panel shows just the southern portion.

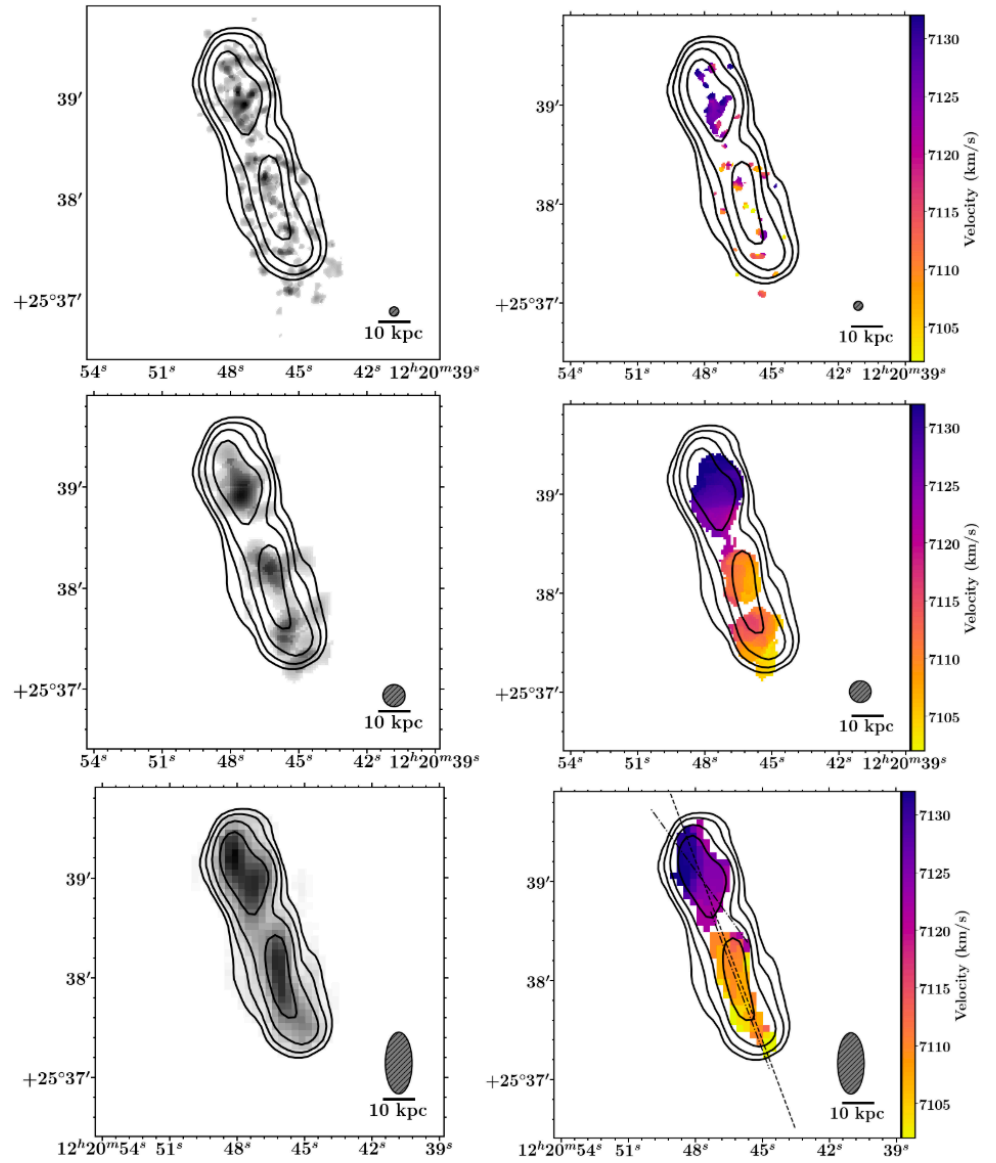

Figure 2. Left panels: H I moment zero column density maps at high- (top: 5.5″ beam), mid- (center: 13.1″ beam) and low-resolutions (bottom: 16×37″ beam). The high and mid resolution maps are from combined VLA B-array and WSRT imaging, and the low resolution map is from WSRT only, Briggs r=0.4 imaging. Beam sizes are shown with hashed gray circles in the lower right on each plot. The column density scale in the top image is 0.5-4.5×10^{20}atoms cm^{-2}, and is 0.15-3.2×10^{20}atoms cm^{-2} in the center image. Column density contours spaced in powers of 2 from 0.2-1.6×10^{20}atoms cm^{-2} from the WSRT moment 0 map are shown on all plots for direct comparison. Moment maps are masked to only include emission detected above 2σ, as discussed in the text. Right panels: Corresponding moment one velocity maps from combined VLA and WSRT (top and center), and WSRT only (bottom), imaging. Resolutions correspond to those of the moment zero maps to the left, masked at the 5σ level to highlight the motions of the highest signal-to-noise gas. The dashed line in the lower right panel shows the location of the position velocity slice shown in Figure 3, and the dot dashed lines show the locations of the northern and southern PV slices in Figure 3.

Table 1. Measured and Derived Properties of AGC 229101

Quantity (units)	Value	Stellar Quantity (units)	Value
RA (h m s, J2000)	12:20:46.8	$\mu_{g,peak}$ (mag arcsec^{-2})	26.58 ± 0.03
Dec (° ′ ″, J2000)	+25:38:24.4	$\mu_{r,peak}$ (mag arcsec^{-2})	26.78 ± 0.06
$V_{h,50}$ (km s^{-1})	7116±4	$m_{g,0}$ (mag)	22.01 ± 0.18
W_{50} (km s^{-1})	43 ± 9	$m_{r,0}$ (mag)	21.58 ± 0.19
Flux (Jy-km s^{-1})	0.78 ± 0.05	$M_{g,0}$ (mag)	−13.11 ± 0.18
Distance (Mpc)	105.9 ± 2.2	$M_{r,0}$ (mag)	−13.55 ± 0.19
$\log_{10}(M_{HI}/M_\odot)$	9.31 ± 0.05	$(g-r)_0$ (mag; large aperture)	0.44 ± 0.26
$N_{HI,peak}$ (10^{20} cm^{-2})	5.1 ± 1.1	$(g-r)_0$ (mag; small aperture)	0.06 ± 0.13
R_{HI} (kpc)	33.5 ± 2.8	V (mag)	21.74 ± 0.24
R_{max} (kpc)	39.6 ± 2.8	B-V (mag; large aperture)	0.65 ± 0.26
M_{HI}/M_*	98^{+111}_{-52}	B-V (mag; small aperture)	0.28 ± 0.12
M_{HI}/L_g ($M_\odot/L_\odot$)	105^{+20}_{-16}	$\log_{10}(M_*/M_\odot)$	7.32 ± 0.33
M_{HI}/L_r ($M_\odot/L_\odot$)	107^{+20}_{-16}	r_h (arcsec)	5.9 ± 1.3
M_{HI}/L_B ($M_\odot/L_\odot$)	110^{+27}_{-23}	r_h (kpc)	3.0 ± 0.7

NOTE— The table lists, in this order: the central position of the H I source, along with measured heliocentric radial velocity, width, and total flux of the H I detection; the estimated distance to the source from the ALFALFA catalog (Haynes et al. 2018); the log of the total mass, column density, and radius of the radio source; the ratio of H I mass to stellar mass; the ratio of H I mass to optical luminosity in the $g-$, $r-$, and B-band filters; the peak surface brightness of the optical counterpart in the g- and r-band; the total apparent and absolute magnitudes of the optical counterpart in the g and r filters; the $g-r$ color of the optical counterpart; the V apparent magnitude and $B-V$ color of the optical counterpart; and the estimated stellar mass and half-light radius (in both arc seconds and kpc) of the optical counterpart. The optical surface brightness values, magnitudes, and colors have been corrected for Galactic extinction by applying the Schlafly & Finkbeiner (2011) coefficients to the reddening values from Schlegel et al. (1998). The peak H I column density is measured in the highest resolution (5.1″ beam) moment 0 map.

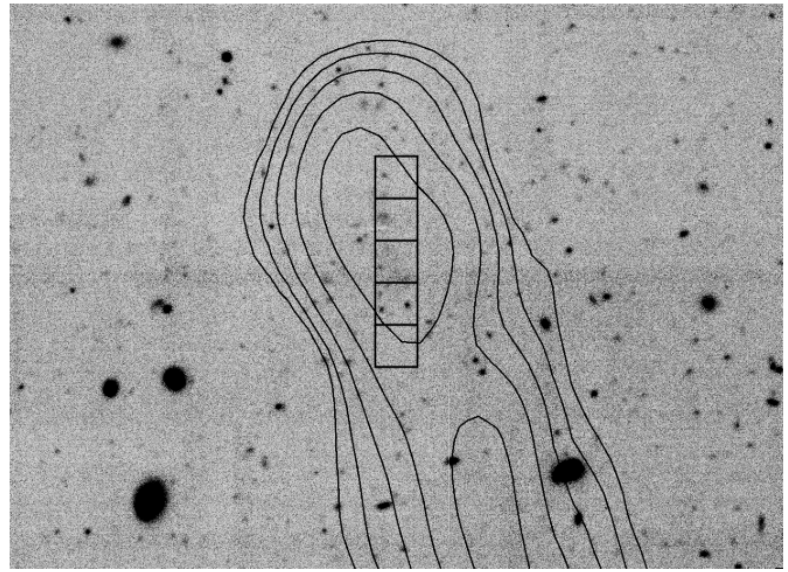

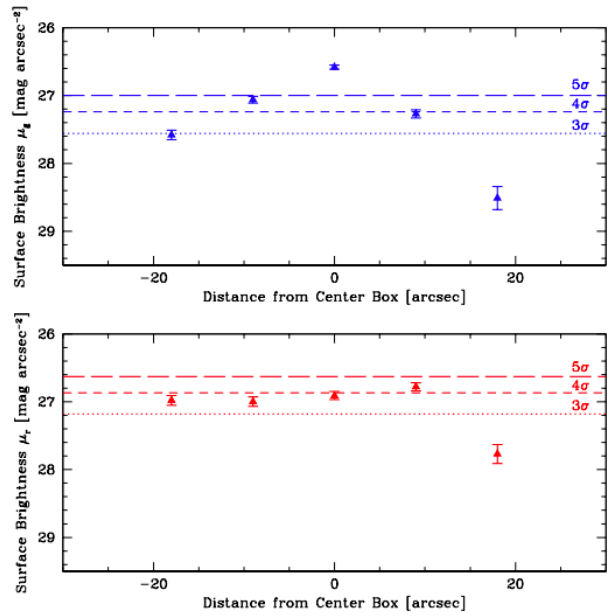

Figure 4. Surface brightness measurements of AGC 229101. The left panel shows a portion of the pODI image that includes the faint optical counterpart that coincides with the northern H I peak; H I contours are again overlaid as in Figure 1. The five square boxes used to calculate surface brightness values of the optical counterpart (see Section 3.2) are also shown. Two discrete sources that appear to be foreground objects (visible in the fourth box from the top) were masked out before the surface brightness measurements were made. The right panel shows the surface brightness values across the object in the g filter (top) and the r filter (bottom). The dotted and dashed lines show the 3-σ, 4-σ, and 5-σ surface brightness detection thresholds in each filter.

Table 1. Measured and Derived Properties of AGC 229101

Quantity (units)	Value	Stellar Quantity (units)	Value
RA (h m s, J2000)	12:20:46.8	$\mu_{g,peak}$ (mag arcsec^{-2})	26.58 ± 0.03
Dec (° ′ ″, J2000)	+25:38:24.4	$\mu_{r,peak}$ (mag arcsec^{-2})	26.78 ± 0.06
$V_{h,50}$ (km s^{-1})	7116±4	$m_{g,0}$ (mag)	22.01 ± 0.18
W_{50} (km s^{-1})	43 ± 9	$m_{r,0}$ (mag)	21.58 ± 0.19
Flux (Jy-km s^{-1})	0.78 ± 0.05	$M_{g,0}$ (mag)	−13.11 ± 0.18
Distance (Mpc)	105.9 ± 2.2	$M_{r,0}$ (mag)	−13.55 ± 0.19
$\log_{10}(M_{HI}/M_\odot)$	9.31 ± 0.05	$(g-r)_0$ (mag; large aperture)	0.44 ± 0.26
$N_{HI,peak}$ (10^{20} cm^{-2})	5.1 ± 1.1	$(g-r)_0$ (mag; small aperture)	0.06 ± 0.13
R_{HI} (kpc)	33.5 ± 2.8	V (mag)	21.74 ± 0.24
R_{max} (kpc)	39.6 ± 2.8	B-V (mag; large aperture)	0.65 ± 0.26
M_{HI}/M_*	98^{+111}_{-52}	B-V (mag; small aperture)	0.28 ± 0.12
M_{HI}/L_g ($M_\odot/L_\odot$)	105^{+20}_{-16}	$\log_{10}(M_*/M_\odot)$	7.32 ± 0.33
M_{HI}/L_r ($M_\odot/L_\odot$)	107^{+20}_{-16}	r_h (arcsec)	5.9 ± 1.3
M_{HI}/L_B ($M_\odot/L_\odot$)	110^{+27}_{-23}	r_h (kpc)	3.0 ± 0.7

NOTE— The table lists, in this order: the central position of the H I source, along with measured heliocentric radial velocity, width, and total flux of the H I detection; the estimated distance to the source from the ALFALFA catalog (Haynes et al. 2018); the log of the total mass, column density, and radius of the radio source; the ratio of H I mass to stellar mass; the ratio of H I mass to optical luminosity in the $g-$, $r-$, and B-band filters; the peak surface brightness of the optical counterpart in the g- and r-band; the total apparent and absolute magnitudes of the optical counterpart in the g and r filters; the $g-r$ color of the optical counterpart; the V apparent magnitude and $B-V$ color of the optical counterpart; and the estimated stellar mass and half-light radius (in both arc seconds and kpc) of the optical counterpart. The optical surface brightness values

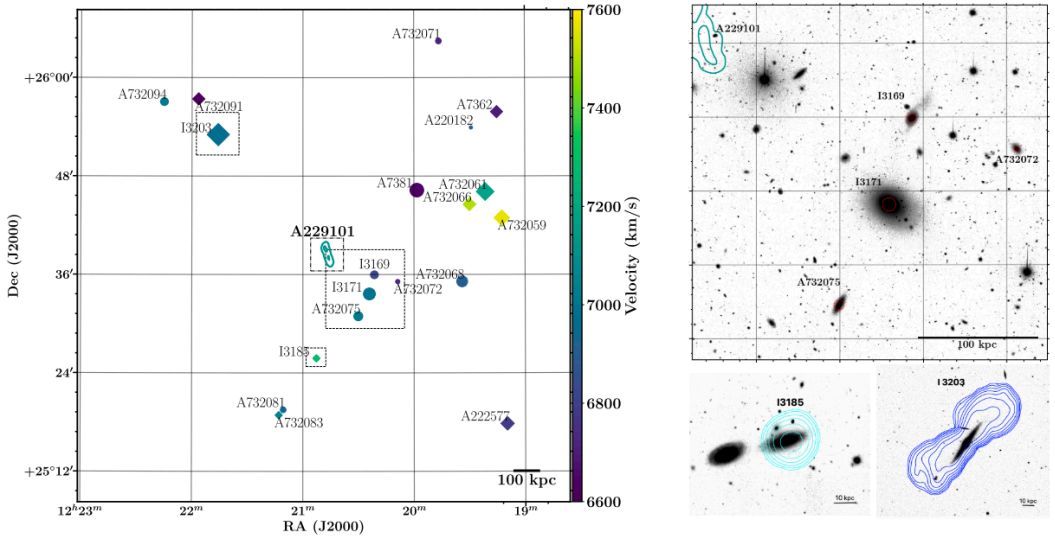

Figure 5. Left: Shown here are galaxies within a projected angular separation of ∼0.5-degree (∼1 Mpc at a distance of 105.9 Mpc), and a recession velocity within 500 km s^{-1}, of AGC 229101's position and velocity. Some of these objects may be possible tidal companions to AGC 229101. The size of each symbol scales with the z-band magnitude of each source, and colors indicate measured recessional velocities as shown in the color bar. Sources with detected H I are marked with diamonds and sources without an H I detection are marked with circles. AGC 229101 is plotted with its H I contours at the center of the figure. The region depicted in Figure 1 is indicated with a dash-dot line, and the regions depicted in the right hand panels are depicted with dashed lines. Right Top: pODI image of IC 3171 and surrounding galaxies to the southwest of AGC 229101. The location of AGC 229101 is indicated by its H I contours in the upper left corner of the figure. Right Bottom: pODI image of IC 3185 with WSRT contours overlaid in light blue, and SDSS image of IC 3203 with WSRT contours overlaid in blue. Note that IC 3203 is outside the FWHM of the WSRT primary beam, but is still bright enough to be detected. WSRT contours for both images range from 1-32×10^{19}atoms cm^{-2} in powers of 2, and have been primary beam corrected.

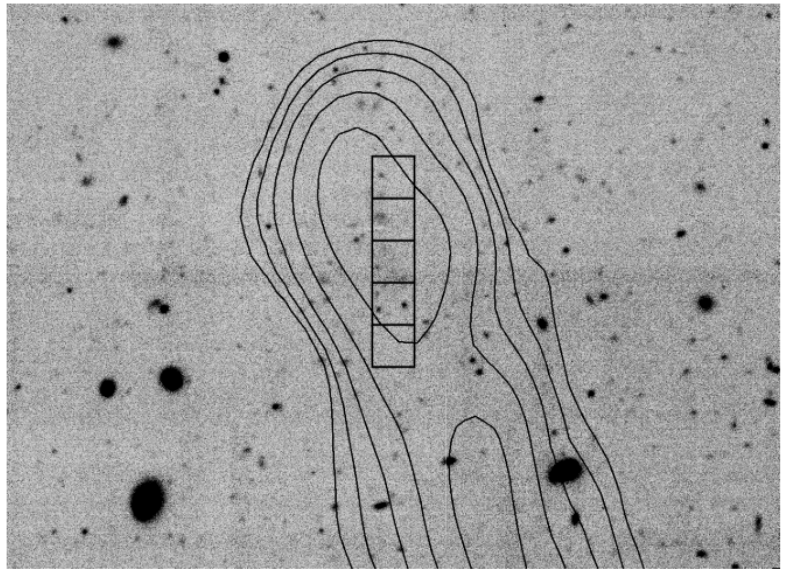

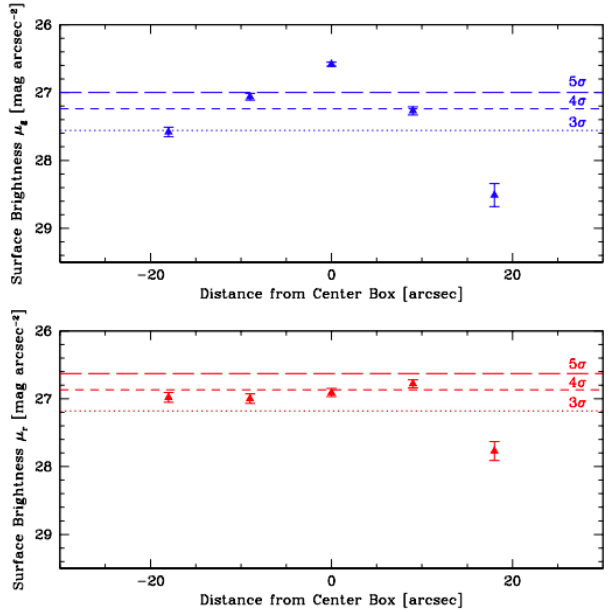

Figure 4. Surface brightness measurements of AGC 229101. The left panel shows a portion of the pODI image that includes the faint optical counterpart that coincides with the northern H I peak; H I contours are again overlaid as in Figure 1. The five square boxes used to calculate surface brightness values of the optical counterpart (see Section 3.2) are also shown. Two discrete sources that appear to be foreground objects (visible in the fourth box from the top) were masked out before the surface brightness measurements were made. The right panel shows the surface brightness values across the object in the g filter (top) and the r filter (bottom). The dotted and dashed lines show the 3-σ, 4-σ, and 5-σ surface brightness detection thresholds in each filter.

Находится в филаментарной области Сверхскопления Coma, между скоплением Coma и скоплением Leo.

Ближайшая галактика с HI – IC3185 с M_{HI}/M_{sun} = 9.52, на 390кпк, deltaV~100км/с

Следующая – IC3203 с M_{HI}/M_{sun} = 10.11, на 610кпк

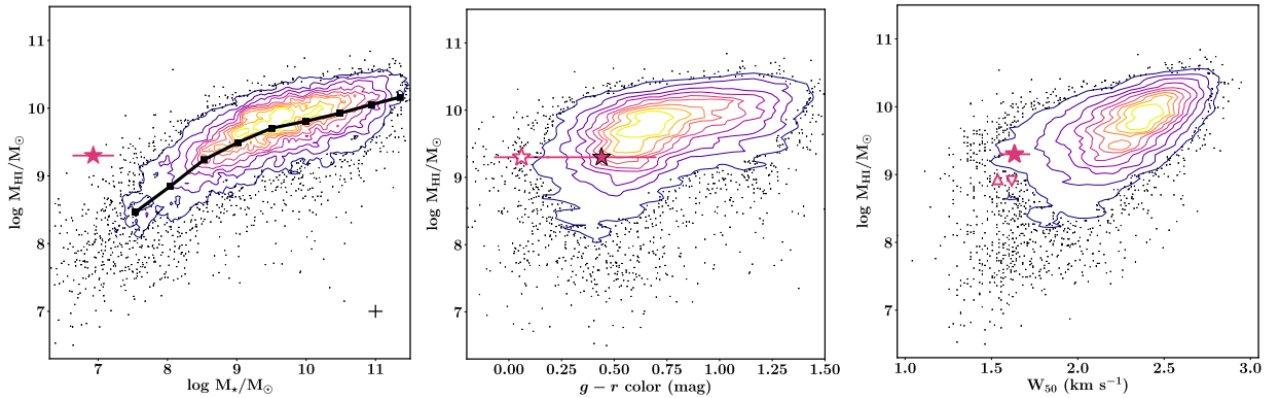

Figure 6. AGC 229101 compared with ALFALFA galaxies from Huang et al. (2012). Contours represent ALFALFA sources as measured by Huang et al. (2012) in 10% intervals from 10% to 90%, with outliers shown by grey dots. Left: H I-mass – stellar mass relation for ALFALFA sources, with stellar masses derived from SED fitting best suited to nearby, gas rich galaxies, as described in Huang et al. (2012). The median relation is shown in black, and typical uncertainties are shown by a black cross in the lower right corner. AGC 229101 is shown as a filled star symbol far off the relation. Note that the stellar mass for AGC 229101 plotted here is the stellar mass derived by matching to the Huang et al. (2012) masses as discussed in Section 3.2.3. Further note that only including gas in the northern component of AGC 229101 reduces the H I mass by 0.3 dex, but still is extreme compared to extrapolation of the median ALFALFA sample. Center: H I-mass versus g–r color for ALFALFA galaxies, compared with AGC 229101. The two measured colors (for two different apertures; see Section 3.2.2) are shown as filled and unfilled symbols and plotted with error bars, which overlap. Right: H I-mass versus H I line width measured at the 50% flux level. The upward pointing triangle represents the northern H I peak, and the downward pointing triangle the southern H I peak. The line width for A229101 – the entire source and the individual peaks – is very narrow relative to the ALFALFA sample.

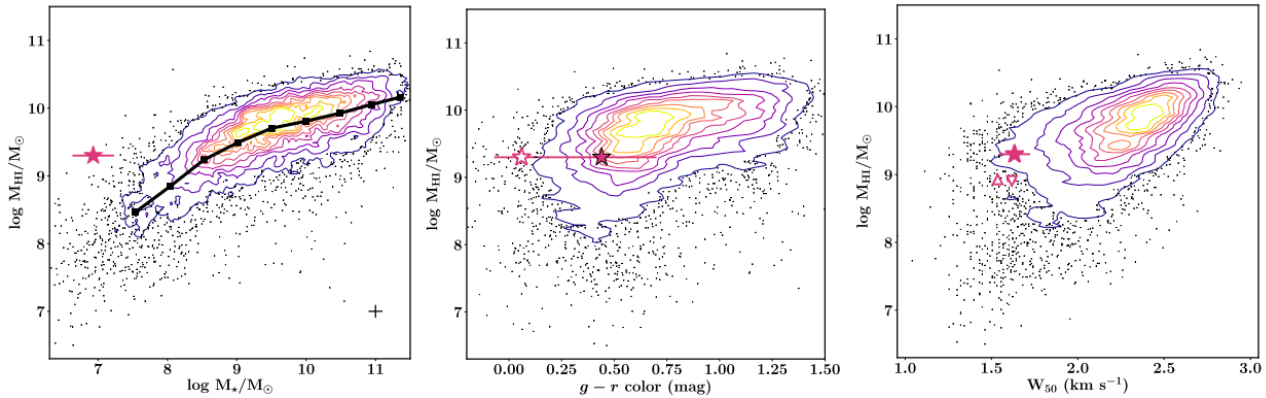

Figure 6. AGC 229101 compared with ALFALFA galaxies from Huang et al. (2012). Contours represent ALFALFA sources as measured by Huang et al. (2012) in 10% intervals from 10% to 90%, with outliers shown by grey dots. Left: H I-mass – stellar mass relation for ALFALFA sources, with stellar masses derived from SED fitting best suited to nearby, gas rich galaxies, as described in Huang et al. (2012). The median relation is shown in black, and typical uncertainties are shown by a black cross in the lower right corner. AGC 229101 is shown as a filled star symbol far off the relation. Note that the stellar mass for AGC 229101 plotted here is the stellar mass derived by matching to the Huang et al. (2012) masses as discussed in Section 3.2.3. Further note that only including gas in the northern component of AGC 229101 reduces the H I mass by 0.3 dex, but still is extreme compared to extrapolation of the median ALFALFA sample. Center: H I-mass versus g–r color for ALFALFA galaxies, compared with AGC 229101. The two measured colors (for two different apertures; see Section 3.2.2) are shown as filled and unfilled symbols and plotted with error bars, which overlap. Right: H I-mass versus H I line width measured at the 50% flux level. The upward pointing triangle represents the northern H I peak, and the downward pointing triangle the southern H I peak. The line width for A229101 – the entire source and the individual peaks – is very narrow relative to the ALFALFA sample.

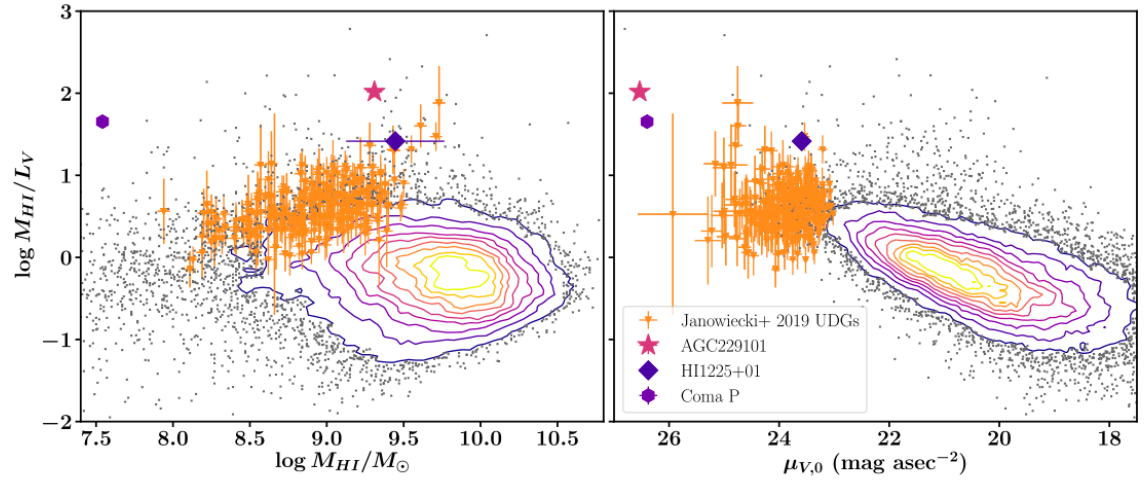

Figure 7. AGC 229101 compared with ALFALFA H I-bearing ultra-diffuse galaxies, and other extreme sources, demonstrating the anomalous nature of AGC 229101 in this parameter space. The panels show the H I-mass – V-band luminosity ratio vs H I-mass (left) and V-band peak surface brightness (right). Contours represent ALFALFA sources as measured with SDSS photometry (see, e.g., Haynes et al. 2011, 2018) increasing in 10% intervals, with outliers shown with small grey points (note: the most extreme outliers have poor optical photometry, as discussed in Section 4.1). ALFALFA Ultra-diffuse galaxies from Leisman et al. 2017 and Janowiecki et al. (2019) are shown with orange triangles, and the extreme ALFALFA sources Coma P and HI1225+01 discussed in the text are shown as a purple hexagon and blue diamond respectively. AGC 229101 is shown as a filled pink star, far lower surface brightness and higher gas fraction than almost all other ALFALFA galaxies. Note that the error bars on AGC 229101 are the size of or smaller than the marker.

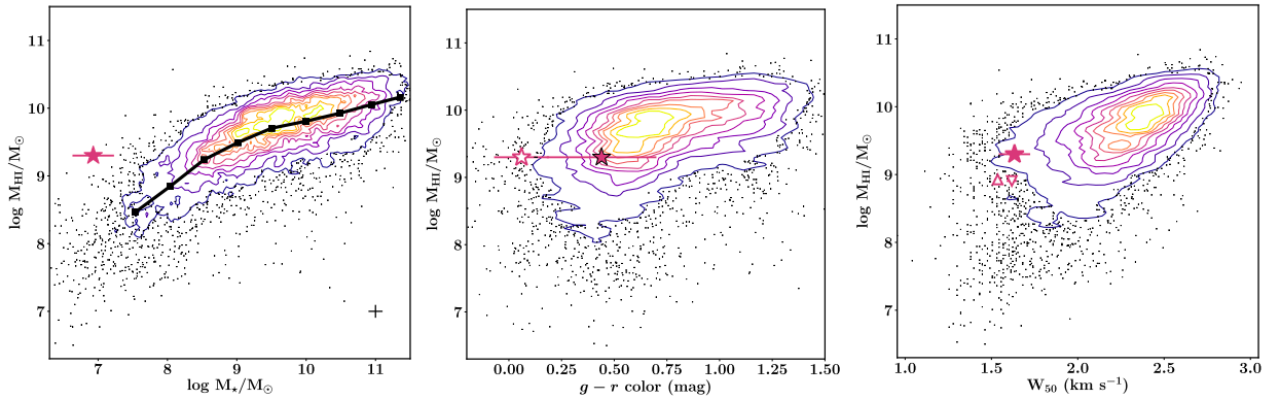

Figure 6. AGC 229101 compared with ALFALFA galaxies from Huang et al. (2012). Contours represent ALFALFA sources as measured by Huang et al. (2012) in 10% intervals from 10% to 90%, with outliers shown by grey dots. Left: H I-mass – stellar mass relation for ALFALFA sources, with stellar masses derived from SED fitting best suited to nearby, gas rich galaxies, as described in Huang et al. (2012). The median relation is shown in black, and typical uncertainties are shown by a black cross in the lower right corner. AGC 229101 is shown as a filled star symbol far off the relation. Note that the stellar mass for AGC 229101 plotted here is the stellar mass derived by matching to the Huang et al. (2012) masses as discussed in Section 3.2.3. Further note that only including gas in the northern component of AGC 229101 reduces the H I mass by 0.3 dex, but still is extreme compared to extrapolation of the median ALFALFA sample. Center: H I-mass versus g–r color for ALFALFA galaxies, compared with AGC 229101. The two measured colors (for two different apertures; see Section 3.2.2) are shown as filled and unfilled symbols and plotted with error bars, which overlap. Right: H I-mass versus H I line width measured at the 50% flux level. The upward pointing triangle represents the northern H I peak, and the downward pointing triangle the southern H I peak. The line width for A229101 – the entire source and the individual peaks – is very narrow relative to the ALFALFA sample.

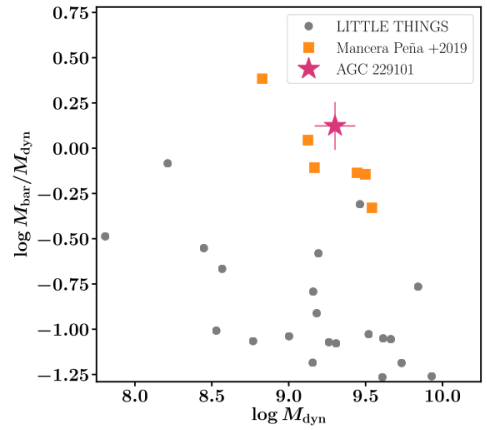

Figure 8. Baryon to dynamical mass fraction versus dynamical mass for AGC 229101 (pink star) compared to the ALFALFA UDG sample from Mancera Piña et al. (2019), and dwarf galaxies from LITTLE THINGS. While AGC 229101 has a larger gas fraction and lower surface brightness than the Mancera Piña et al. (2019) sample, it appears to have similarly high baryonic mass for its rotation velocity; within R_{HI} AGC 229101 requires no additional dark matter component.

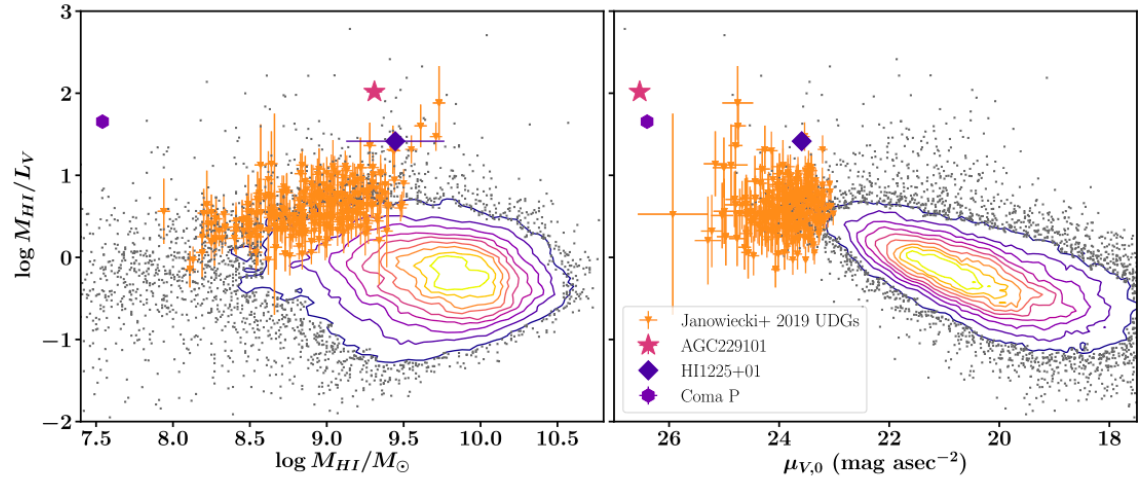

Figure 7. AGC 229101 compared with ALFALFA H I-bearing ultra-diffuse galaxies, and other extreme sources, demonstrating the anomalous nature of AGC 229101 in this parameter space. The panels show the H I-mass – V-band luminosity ratio vs H I-mass (left) and V-band peak surface brightness (right). Contours represent ALFALFA sources as measured with SDSS photometry (see, e.g., Haynes et al. 2011, 2018) increasing in 10% intervals, with outliers shown with small grey points (note: the most extreme outliers have poor optical photometry, as discussed in Section 4.1). ALFALFA Ultra-diffuse galaxies from Leisman et al. 2017 and Janowiecki et al. (2019) are shown with orange triangles, and the extreme ALFALFA sources Coma P and HI1225+01 discussed in the text are shown as a purple hexagon and blue diamond respectively. AGC 229101 is shown as a filled pink star, far lower surface brightness and higher gas fraction than almost all other ALFALFA galaxies. Note that the error bars on AGC 229101 are the size of or smaller than the marker.

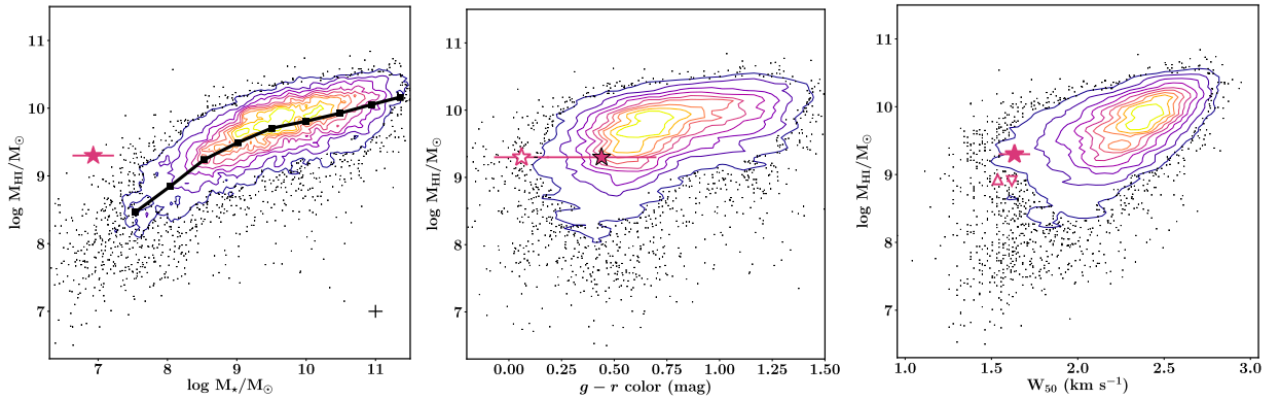

Figure 6. AGC 229101 compared with ALFALFA galaxies from Huang et al. (2012). Contours represent ALFALFA sources as measured by Huang et al. (2012) in 10% intervals from 10% to 90%, with outliers shown by grey dots. Left: H I-mass – stellar mass relation for ALFALFA sources, with stellar masses derived from SED fitting best suited to nearby, gas rich galaxies, as described in Huang et al. (2012). The median relation is shown in black, and typical uncertainties are shown by a black cross in the lower right corner. AGC 229101 is shown as a filled star symbol far off the relation. Note that the stellar mass for AGC 229101 plotted here is the stellar mass derived by matching to the Huang et al. (2012) masses as discussed in Section 3.2.3. Further note that only including gas in the northern component of AGC 229101 reduces the H I mass by 0.3 dex, but still is extreme compared to extrapolation of the median ALFALFA sample. Center: H I-mass versus g–r color for ALFALFA galaxies, compared with AGC 229101. The two measured colors (for two different apertures; see Section 3.2.2) are shown as filled and unfilled symbols and plotted with error bars, which overlap. Right: H I-mass versus H I line width measured at the 50% flux level. The upward pointing triangle represents the northern H I peak, and the downward pointing triangle the southern H I peak. The line width for A229101 – the entire source and the individual peaks – is very narrow relative to the ALFALFA sample.

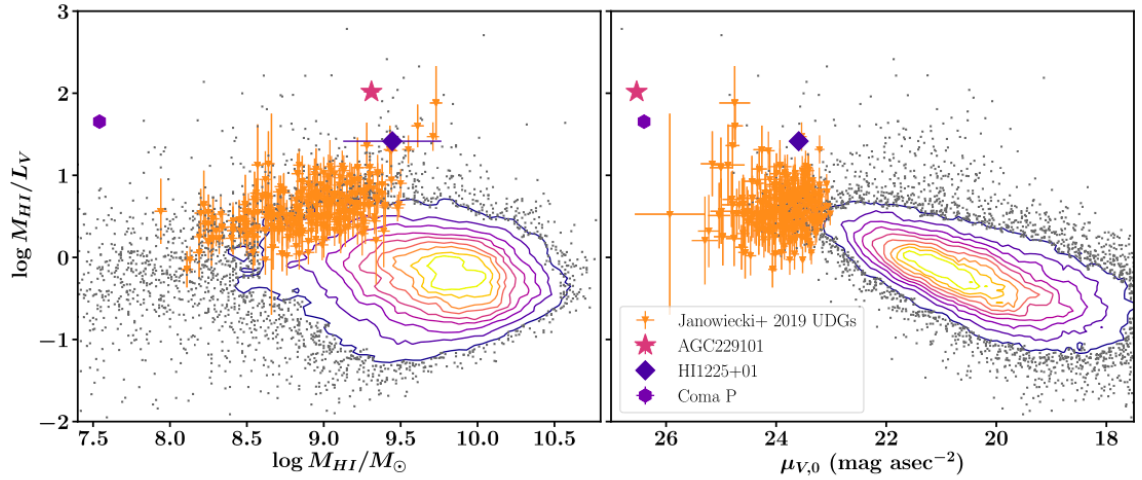

Figure 7. AGC 229101 compared with ALFALFA H I-bearing ultra-diffuse galaxies, and other extreme sources, demonstrating the anomalous nature of AGC 229101 in this parameter space. The panels show the H I-mass – V-band luminosity ratio vs H I-mass (left) and V-band peak surface brightness (right). Contours represent ALFALFA sources as measured with SDSS photometry (see, e.g., Haynes et al. 2011, 2018) increasing in 10% intervals, with outliers shown with small grey points (note: the most extreme outliers have poor optical photometry, as discussed in Section 4.1). ALFALFA Ultra-diffuse galaxies from Leisman et al. 2017 and Janowiecki et al. (2019) are shown with orange triangles, and the extreme ALFALFA sources Coma P and HI1225+01 discussed in the text are shown as a purple hexagon and blue diamond respectively. AGC 229101 is shown as a filled pink star, far lower surface brightness and higher gas fraction than almost all other ALFALFA galaxies. Note that the error bars on AGC 229101 are the size of or smaller than the marker.

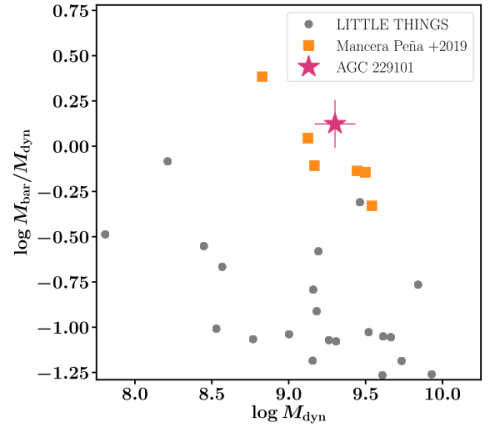

Figure 8. Baryon to dynamical mass fraction versus dynamical mass for AGC 229101 (pink star) compared to the ALFALFA UDG sample from Mancera Piña et al. (2019), and dwarf galaxies from LITTLE THINGS. While AGC 229101 has a larger gas fraction and lower surface brightness than the Mancera Piña et al. (2019) sample, it appears to have similarly high baryonic mass for its rotation velocity; within R_{HI} AGC 229101 requires no additional dark matter component.

Возможные механизмы:

1. Приливной карлик (но расстояние до ближайших соседей относительно большое, и нет никаких следов приливных хвостов)
2. Механизмы, которые рассматриваются для формирования UDG?
3. Сливающиеся темные облака
4. AGC229101 – изолированная протяженная галактика низкой поверхностной яркости с небольшим темным гало

Void Galaxy Distribution: A Challenge for ΛCDM

Saeed Tavasoli
Physics Department, Kharazmi University, Tehran, Iran; tavasoli@ipm.ir

Abstract

We extract void catalogs from the Sloan Digital Sky Survey Data Release 16 (SDSS DR16) survey and also from the Millennium simulation. We focus our comparison on distribution of galaxies brighter than $M_r < -18$ inside voids and study the mean separation of void galaxies, distance from the void center, and the radial density profile. We find that mean separation of void galaxies depends on void size, as bigger voids have lower mean separation in both samples. However, void galaxies in the observation sample seem to have generally larger mean–distance than simulated ones at any given void size. In addition, observed void galaxies tend to reside closer to the void center than those in the simulation. This discrepancy is also shown in the density profile of voids. Regardless of the void size, the central densities of real void profiles are higher than the ones in the predicted simulated catalog.

Arxiv: 2109.10369

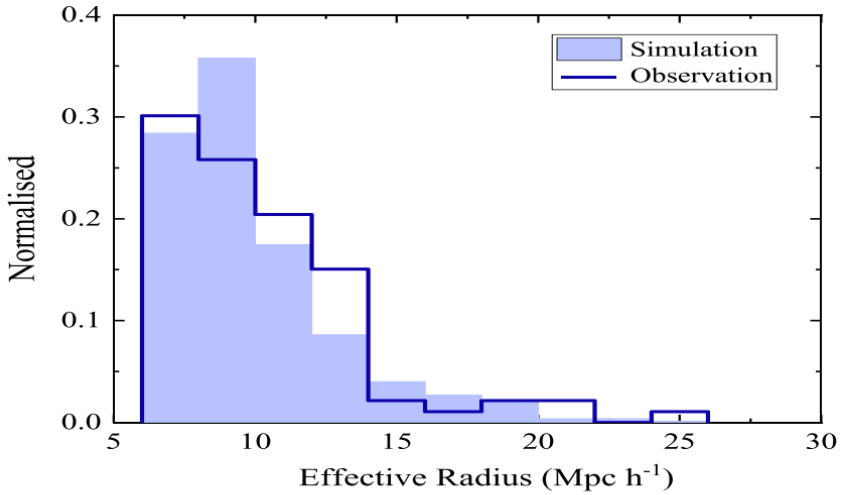

Figure 1. Void size distributions of observation and simulation catalogs.

SDSS (~30000 галактик, выделили ~100 войдов)
Millenium simulation (~5*10^6 галактик, выделили ~18000войдов)
M_r<-18

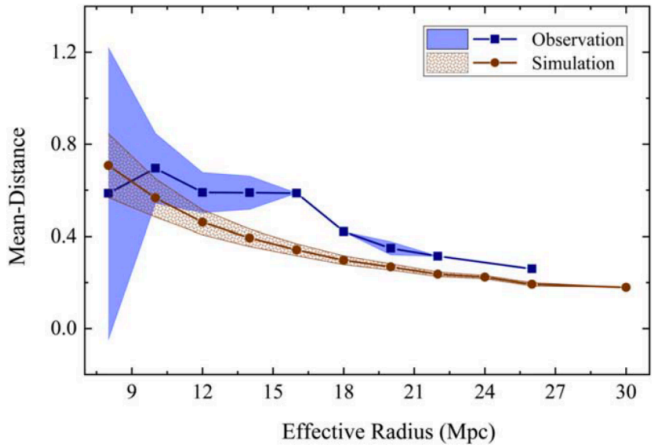

Figure 3. Median mean–distance as a function of void size for observation and simulation sample.

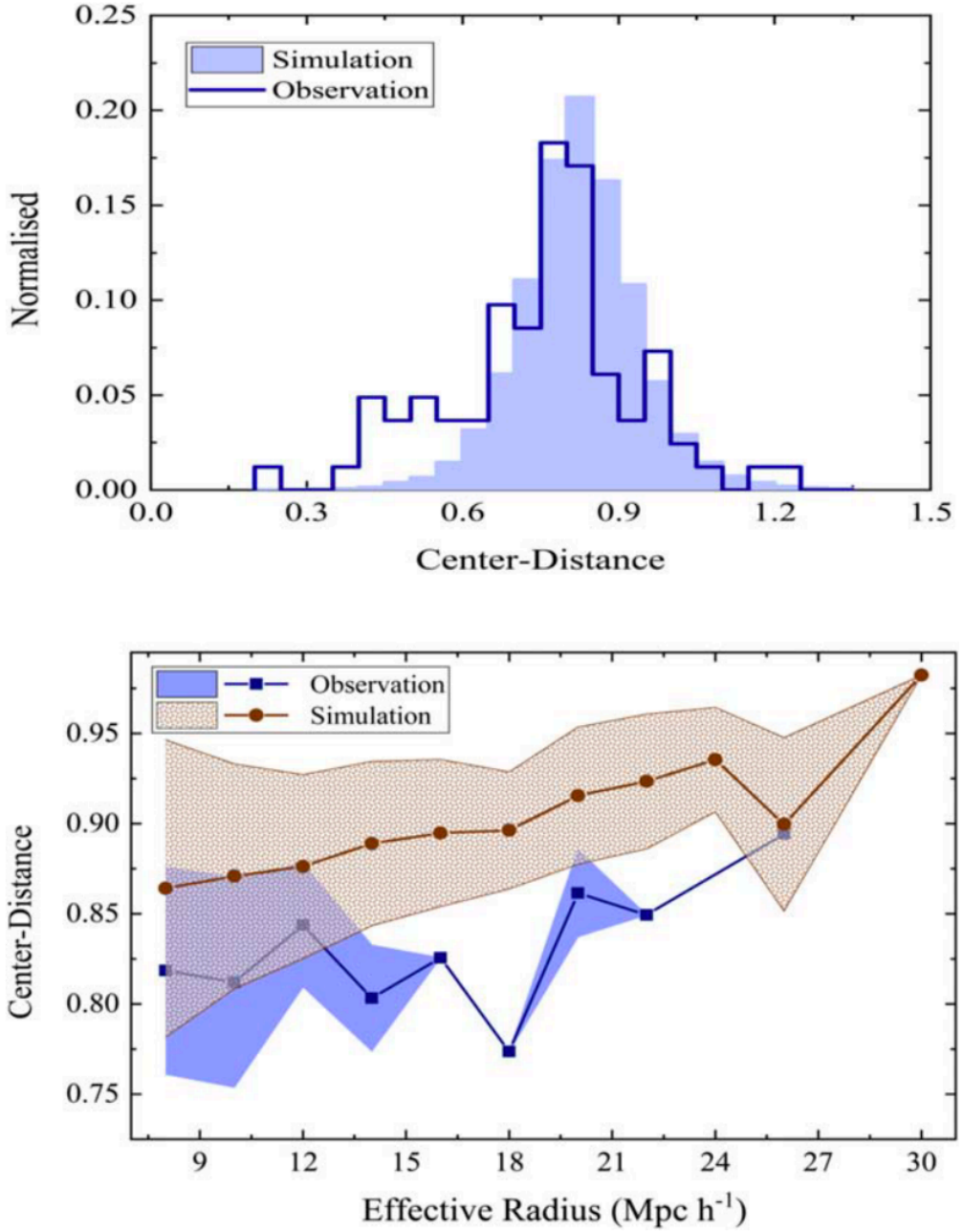

Figure 2. Center–distance distributions (top panel) and median center–distance as a function of void size (bottom panel) for the observation and simulation samples.

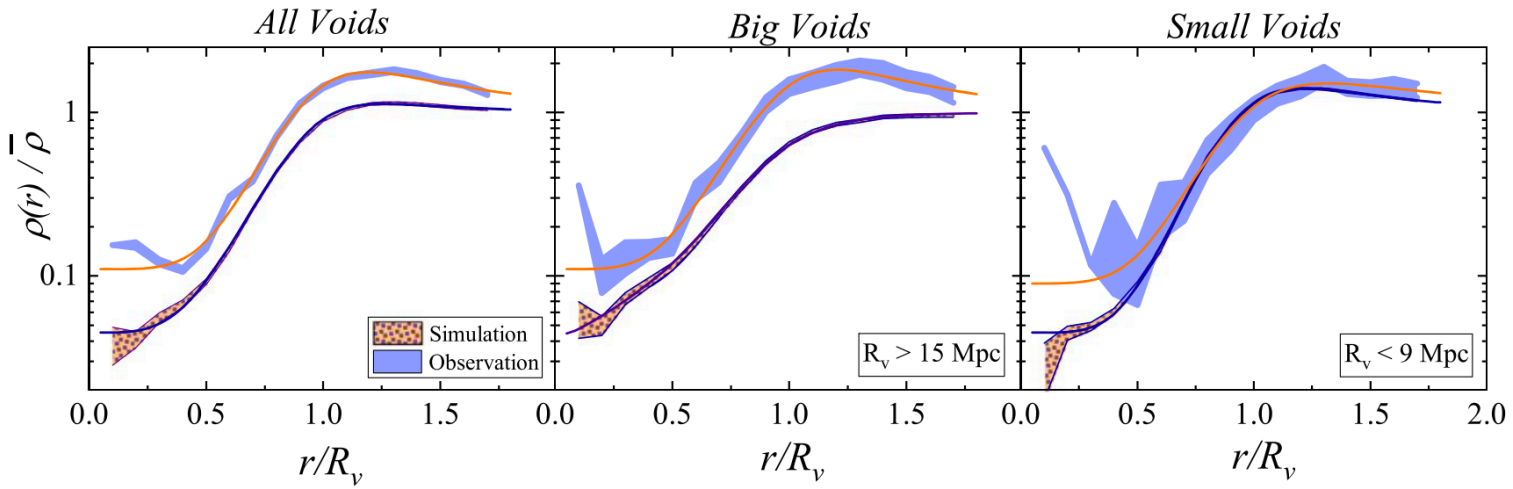

Figure 5. Average stacked density profiles drawn from *All-voids* (left panel), *Big-voids* (middle panel) and *Small-voids* (right panel) identified in the SDSS and simulation sample. Shaded regions depict the standard deviation 1σ within each of the stacks and the solid colored lines indicate the best fits for each curve.

Наблюдения и результаты моделирования не сходятся!

Правда, у других авторов получаются иные параметры войдов (другие алгоритмы выделения войдов, методики измерения средних профилей, другие выборки…), так что надо разбираться.